Numerical simulation of Submarine non-rigid landslide by an explicit three-step incompressible smoothed particle hydrodynamics

Seyed Erfan Hosseini Mobara[1], Rasool Ghobadian[2*], Fardin Rouzbahani[3] , Dejana Đorđević[4]

[1] Postdoctoral research fellow in Hydraulic Structures Enginerring, Department of Water Engineering, Razi University, Kermanshah 67144-14971, Iran.
[2] Associate professor, Department of Water Engineering, Razi University, Kermanshah 67144-14971, Iran.
[3] Assistant professor, Department of Mechanical Engineering, Islamic Azad University, Hamedan 15743-65181, Iran.

[4] Assistant professor ,University of Belgrade, Faculty of Civil Engineering, Department of Hydraulic and Environmental Engineering, Belgrade, Serbia

*Corresponding author: Rasool Ghobadian (rsghobadian@gmail.com), Tel.:+98 918-833-2489, Fax: +98 833-832-4820.

Abstract

Many landslides in nature may be classified as deformable landslides. The landslide volume is usually modeled as a rheological material when SPH methods are used for landslide simulation, since these methods allow for the use of particles with different fluid properties. To increase the accuracy, the Carreau-Yasuda model is chosen in this study to predict the behavior of the rheological material. This rheological model overcomes the weakness of the power-law model in predicting the viscosity at zero and infinite shear strain rates. Also, a fully explicit three-step algorithm is proposed to solve the governing equations. In *the first step*, the momentum equation is solved in the presence of the body forces while neglecting all other forces. In this step intermediate velocity values are computed. In *the second step*, the calculated intermediate velocities are employed to compute divergence of the stress tensor, and velocity components of each particle are updated to find their intermediate positions. These two steps are called predictor steps. In *the third, corrector step*, the pressure gradient in the momentum equation is merged with the continuity equation, and lastly the final particle velocity is calculated at the end of the time step. The fully explicit three-step algorithm is used in combination with Carreau-Yasuda model to simulate the submarine non-rigid landslide from the physical model. The comparison with the experimental data indicates good agreement between the calculated and observed water surface elevations with very low L2 relative error norm (ε_{L2}) and *RMSE* values that are up to 70% lower than those from previous studies when Cross and Bingham rheological models were used with ISPH and WCSPH models, respectively. Moreover, the shape and the advancement of the non-rigid body made of sand are captured equally good.

Keywords: Smoothed particle hydrodynamics; Non-Newtonian fluid; Carreau-Yasuda model, Submarine landslide; Lagrangian method

1. Introduction

Huge waves on the water surface like Tsunamis are triggered by a sudden disturbance of the ocean floor or on the ocean surface. Such a disturbance is usually caused by an earthquake, a landslide, a volcanic eruption and other types of underwater explosions (including detonations of underwater nuclear devices), glacier calving, meteorite impacts, or other disturbances above or below water surface which have the potential to generate a tsunami [1-3]. Failure of a breakwater during tsunami causes extensive damages to human lives and properties. Therefore, it is essential to investigate the failure mechanisms of a breakwater due to a tsunami.

Landslides are among the most catastrophic and very frequent hazards around the world. Slope failures and subsequent landslides on the margins of a dam reservoir can generate large impulsive waves, which may lead to a significant damage to a dam body, agricultural area, shoreline properties and lives [4, 5]. Therefore, the impulsive waves are considered as one of the notable secondary hazards induced by landslides [6].

Depending on the location of the landslide, there are three types of waves: those induced by submarine landslides, those induced by partially submerged landslides, and those induced by subaerial landslides [7-9]. Depending on the depth of the receiving water body, the landslide may be either completely or only partly submerged after its deposition. The formation, propagation and run-up of landslide induced impulse waves have been studied through simple physical experiments [7, 8, 10], analytical formulae [11], scale-model physical experiments [12] and numerical simulation [4, 13-16].

In terms of the used mathematical formulation, models can be categorized into one of the following three categories: 1) the Boussinesq-type models [17-19], 2) the shallow water equations (SWEs) models [20] and 3) the fully Navier-Stokes (N-S) models [21, 22]. In particular, the SWEs models are widely accepted to solve the wave propagation problem with the numerical schemes such as the finite element method (FEM) and the finite volume method (FVM) [20, 23-25].

Recently, mesh-free methods have been given special attention in simulating problems, whose solution may be sought using numerical procedures which do not require a computational grid. Such methods improve the flexibility of the code on one hand, and bring new numerical problems to be solved, on the other. The main advantage of meshless descriptions comes out when dealing with moving boundaries and large deformations. Development of mesh-free methods offers an opportunity to overcome either of the two problems. One of these methods is the so-called smoothed particle hydrodynamics method, which is a widely spread meshfree numerical tool.

A particle method does not need grid for calculating field properties. A particle is, like a node in the FEM, a calculation unit. The method uses a weighting function to get properties from the neighboring particles. The weighting function is usually related to the inverse distance to the surrounding particles. The number of neighboring particles is decided by the influence domain that is redefined in every step. As a result, the particle method can easily simulate free surface flow in fluids and allow large deformations in solids. The result obtained with the particle method is usually not as accurate as that obtained with s a grid-based method such as FEM. The SPH method introduced by Gingold and Monaghan, 1977 [26] (and separately by Lucy, 1977 [27]) is better than any other particle method in terms of accuracy. It was developed to solve astronomical problems, but soon afterwards it became a powerful tool in fluid flow simulations. Wave overtopping characteristics that were simulated by Shao et al., 2006 [28] and Pu and Shao, 2012 [29] proved the ability of SPH to simulate such violent flows. Modeling of stress wave propagation and uniaxial/ triaxial test by Das and Cleary, 2006 [30] and Das and Cleary, 2007 [31] has proved the robustness of the SPH method in simulating solid mechanics problems. Fluid-structure interaction was simulated by Antoci et al., 2007 [32] with reasonable accuracy, which proved the strength of the SPH method as a coupling tool. Naili et al. [33] have simulated liquefaction induced lateral spreading by the SPH using the Bingham soil model. A seepage flow analysis by Maeda et al., 2006 [34] was the first attempt to simulate geo-material with the SPH. Maeda et al., 2006 [34] have simulated failure of soil by taking into account soil-water-air interaction. Simulation of seepage and erosion with the evolution of air bubbles by Sakai and Maeda, 2009 [35] was the symbol of the SPH advancement in geo-technics. Takbiri et al., 2010 [36] have performed seepage analysis through the dam foundation by SPH and compared results with FEM. Bui et al., 2011 [37] have developed a SPH model for seepage flow through deformable porous media where the deformation of geo-material was simulated. Simulations of large deformation of geo-material with elasto-plastic D-P constitutive model by Bui et al., 2008a [38] was a milestone of the SPH applications in geotechnical engineering. Bui et al., 2008b [39] also analysed soil-structure interaction by simulating the interaction of flowing geo-materials with the pile structures. Slope stability analysis and discontinuous slope failure analysis by Bui et al., 2011b [40] and simulation of saturated soil with improved consideration for pore water pressure by Bui and Fukagawa, 2013 [41] are additional proofs of the SPH

ability to handle large deformation of geo-material. Chen and Qiu, 2011 [42] simulated 3-D granular flow by the SPH method. Opez et al., 2012 [43] have improved the accuracy of the granular flow by using different particle sizes in the simulation termed as dynamic refinement. Hiraoka et al., 2013 [44] have simulated slope failure due to the effect of seismic motion by the SPH. Nguyen et al., 2013 [45] have simulated the behavior of modular block retaining wall. Lemiale et al., 2012 [46] have simulated landslide event by combining SPH with the discrete element method (SPH-DEM method). The SPH was used to simulate the onset of the landslide, while the subsequent flow was simulated by the DEM. Wang et al., 2013 [47] have developed a new frictional contact to simulate movement of the retaining wall and consequent soil pressure by the SPH.

It is well known that Newtonian fluids are fluids that obey Newton's linear law of friction:

$$\tau = \mu\dot{\gamma} \tag{1}$$

where τ is the shear stress, μ is the dynamic viscosity of the fluid expressed in Ns / m^2 = Pa s, and the quantity $\dot{\gamma}$ is the rate of shear strain. Dynamic viscosity μ is the proportionality coefficient in this model. Fluids that do not follow this linear law are called non-Newtonian fluids. These fluids are usually highly viscous, and their elastic properties also affect the flow field. The theory of non-Newtonian fluids is a part of rheology. Typical non-Newtonian fluids are polymer solutions, thermoplastics, drilling fluids, paints, fresh concrete and biological fluids [48]. Granular flows caused by soil liquefaction or landslides are also non-Newtonian fluids.

Table 1 summarises recent numerical studies in which the mass of earth or rock in the landslide is treated as a rigid block, while Table 2 summarises those in which the sliding body is treated as a non-Newtonian fluid whose deformation is modeled using the rheological theory.

Table 1
Numerical studies of a rigid landslide

Reference	Simulation method	Impact angle	Landslide shape	Landslide initial position
Heinrich, 1992 [49]	VOF	45	Triangle	SM
Monaghan et al., 2003 [50]	SPH	10	Rectangle	SA
Ataie-Ashtiani and Shobeyri, 2008 [10]	ISPH	45, 90	Triangle, Rectangle	SM
Serrano-Pacheco et al., 2009 [51]	FVM	30.7	Polygon	SA
Wenjie, 2012 [52]	CEL	45	Triangle	SM
Viroulet et al., 2013 [25]	SPH, FVM	35	Trapezoid	SM, PSM
Wang et al., 2016b [53]	DDA-SPH	45	Triangle	SM
Khoolosi and Kabdaşli, 2016 [54]	Flow-3D	45	Circular Sphere Rectangular Cube Triangular prism	SA
Farhadi et al., 2016 [16]	ISPH	45	Triangle	SM
Heller et al., 2016 [55]	SPH (DualSPHysics v3.1)	45	Trapezoid cube	SA
Qiu et al., 2017 [15]	DEM	45	Triangle	SM
Tan et al., 2018 [3]	block DEM-SPH	45	Triangle, Trapezoid cube	SA

SM: submerged; SA: subaerial; PSM: partially submerged; DEM: discrete element method

Table 2
Numerical studies of a non-rigid landslide

Reference	Soil model	Simulation method	Impact angle	Landslide initial position	μ_B(Pa s)	τ_B(Pa)
Rzadkiewicz et al., 1997 [56]	BM	VOF	45	SM	0	200
					0	1000
Mariotti and Heinrich, 1999 [57]	BM	VOF	45	SM	0	Update
Quecedo et al., 2004 [21]	Generalized viscoplastic fluid model	CBG	45	SA	48	1000
Ataie-Ashtiani and Shobeyri, 2008 [10]	BM and Cross model	ISPH	45	SM	0.1	250
					0.15	750

Capone et al., 2010 [58]	Changed BM	SPH	45	SM	1	1000
Shi et al., 2016 [59]	elasto–plastic material	soil–water coupling SPH	45	SA	-	-
Qiu et al., 2017 [15]	Combining the Papanastasiou and HB model	SPH	45	SM	0.002	200
					0.002	1000
Wang et al., 2017b [13]	DDA	DDA-SPH	45	SA	-	-
Farhadi, 2018 [1]	BM	ISPH	45	SM	1	1000

SM: submerged; SA: subaerial; PSM: partially submerged; BM: Bingham model; DDA: Discontinuous Deformation Analysis; HB: Herschel-Bulkley model

Significant progress has been made in the context of computational rheology in recent years. Several numerical methods have been devised to study non-Newtonian fluid flows with different degrees of success [60]. More specifically, Galerkin-type finite element methods have been used to analyse Bingham-plastic fluids, but they have shown appreciable errors in the calculated shear rates and viscosities [60]. On the other hand, non-Newtonian Carreau-Yasuda fluids that belong to the Pseudoplastic fluid family have been successfully used in simulations of non-rigid bodies such as sand [61].

Thus far, little attention has been paid to the investigation of the particle's movement on rigid slopes due to landslides, collapses or falls of non-rigid bodies down rigid slopes as well as on the propagation of the resulting waves on the free surface. Innovations in the present paper are twofold. The first one is a modification of the SPH method through an introduction of the three-step procedure to facilitate non-Newtonian flow modeling. The second one is an introduction of the non-Newtonian Carreau-Yasuda fluid into the SPH model to facilitate simulation of sliding of the non-rigid, granular body down a rigid slope. To the authors' best knowledge lanslides have not yet been simulated as granular bodies whose grains carry characteristics of the two-phase fluid flow themselves.

2. Governing equations

2.1. Conservation laws in Lagrangian framework

The mass and momentum conservation laws for the unsteady incompressible fluid flow in the Lagrangian framework can be written as follows [26]:

$$\nabla \cdot \mathbf{V} = 0 \tag{2}$$

$$\frac{\mathrm{D}\mathbf{V}}{\mathrm{D}t} = -\frac{1}{\rho}\nabla P + \mathbf{g} + \frac{1}{\rho}\nabla \cdot \tau \tag{3}$$

where time t is the independent variable, $\mathbf{g}$ is the vector of gravitational acceleration, ρ is the density, P is the pressure, $\mathbf{V}$ is the velocity vector, τ is the shear stress tensor and $\mathrm{D}/\mathrm{D}t$ refers to the material derivative.

2.2. *Fundamentals of the SPH method*

The integral expression of a variable A, which is a function of spatial coordinates, can be presented as [62, 63]:

$$A(\boldsymbol{r}) = \int_{\Omega(\boldsymbol{r})} A(\boldsymbol{r}')\delta(|\boldsymbol{r}-\boldsymbol{r}'|)\mathrm{d}\boldsymbol{r}' \approx \langle A(\boldsymbol{r})\rangle = \int_{\Omega(\boldsymbol{r})} A(\boldsymbol{r}')\, W_h(|\boldsymbol{r}-\boldsymbol{r}'|)\mathrm{d}\boldsymbol{r}' \tag{4}$$

where, $\delta(|\boldsymbol{r}-\boldsymbol{r}'|)$ is the Dirac delta function, $\mathrm{d}\boldsymbol{r}'$ is the volume differential element, $W_h(|\boldsymbol{r}-\boldsymbol{r}'|) = W(|\boldsymbol{r}-\boldsymbol{r}'|, h)$ is the Kernel interpolation function with a smoothing length h. The integration is performed in the supporting domain $\Omega(\boldsymbol{r})$. Since the Kernel interpolation function decreases rapidly with distance from the particle a, this integral can be approximated with a sum over neighbouring particles as follows [62, 63]:

$$A_i = A(\boldsymbol{r}_i) = \sum_j \frac{m_j}{\rho_j} A_j\, W\left(\left|\boldsymbol{r}_i - \boldsymbol{r}_j\right|, h\right) \tag{5}$$

Typically, the smoothing length h is chosen to be of the size of particle intervals.

The interpolation (Kernel) functions that are used in this method should satisfy the following special conditions [64]:

$$\int W_h(|\boldsymbol{r}-\boldsymbol{r}'|)\mathrm{d}\boldsymbol{r}' = 1 \tag{6}$$

$$W_h(|\boldsymbol{r}-\boldsymbol{r}'|) = 0 \quad \text{out of the supporting domain} \tag{7}$$

$$\lim_{h\to 0} W_h(|\boldsymbol{r}-\boldsymbol{r}'|) = \delta(|\boldsymbol{r}'-\boldsymbol{r}|) \tag{8}$$

$$W_h(|\boldsymbol{r}-\boldsymbol{r}'|) > 0 \quad \text{within the supporting domain} \tag{9}$$

In this paper, we use the cubic spline Kernel function after Liu and Liu, 2003 [65]:

$$W_h(|\boldsymbol{r}-\boldsymbol{r}'|) = \frac{\beta}{h^d}\begin{cases}(2-q)^3-4(1-q)^3 & 0\le q\le 1\\ (2-q)^3 & 1\le q<2\\ 0 & q>2\end{cases} \tag{10}$$

where $q = |\boldsymbol{r}-\boldsymbol{r}'|/h$, and $\beta = 5/14\pi$ are taken in two-dimensional problems.

The gradient of an arbitrary variable A can be written directly as:

$$(\nabla A)_i = \sum_j \frac{m_j}{\rho_j} A_j \nabla W(\boldsymbol{r}_i - \boldsymbol{r}_j, h) = \sum_j \frac{m_j}{\rho_j} A_j \nabla_i W_{ij} \tag{11}$$

2.3. *Viscous terms*

The viscous term was first introduced into the SPH equations by Lucy in 1977 [27]. However, solutions to many viscous problems with the SPH method became possible with the work of Monaghan and Gingold, 1983 [62].

The viscosity term is introduced into SPH model equations with the second-order derivative term, which is obtained just by differentiating the Kernel interpolation function twice. However, in practice, the second-order derivative terms can be susceptible to the particle's irregularity. This might cause some problems in reaching physically plausible solutions. To avoid this problem, Monaghan and Gingold proposed a different approximation of Eq. (3) [62]:

$$\frac{\mathrm{d}\mathbf{V}_i}{\mathrm{d}t} = -\sum_j m_j\left(\frac{P_i}{\rho_i^2}+\frac{P_j}{\rho_j^2}+\pi_{ij}\right)\nabla_i W_{ij} \tag{12}$$

In the above equation, π_{ab} is added as the viscous pressure. The additional term is also called the artificial viscosity [63].

The primary purpose of adding the artificial viscosity was to model the strong shocks in astrophysical processes ([63]; [66]). Morris et al., 1997 [67] have found that if the artificial viscosity method was used to model real viscous terms, it might give inaccurate velocity profiles in some situations.

The strain rate in Newtonian and non-Newtonian fluids is given by the following relation [68]:

$$\mathbf{D} = \frac{\nabla\mathbf{V}+\nabla\mathbf{V}^T}{2} \tag{13}$$

The shear stress in the incompressible fluid flow is defined as a function of D's second invariant i.e. $|D|$:

$$|\mathbf{D}| = \sqrt{\sum_{i,j}\mathbf{D}_{ij}\mathbf{D}_{ij}} \tag{14}$$

Thus, the relationship between the shear stress and the strain rate for Newtonian and non-Newtonian fluids is expressed as follows:

$$\tau = \mu(|\mathbf{D}|)\mathbf{D} \tag{15}$$

For Newtonian fluids, the previous expression reduces to:

$$\tau = 2\mu\mathbf{D} \tag{16}$$

The two-dimensional velocity gradient vector in Eq. (13) can be written as:

$$\nabla \mathbf{V} = \begin{bmatrix} \dfrac{\partial u}{\partial x} & \dfrac{\partial u}{\partial y} \\ \dfrac{\partial v}{\partial x} & \dfrac{\partial v}{\partial y} \end{bmatrix} \tag{17}$$

Following this, the strain rate **D** is expressed as:

$$\mathbf{D} = \begin{bmatrix} \dfrac{\partial u}{\partial x} & \dfrac{1}{2}\left(\dfrac{\partial u}{\partial y} + \dfrac{\partial v}{\partial x}\right) \\ \dfrac{1}{2}\left(\dfrac{\partial u}{\partial y} + \dfrac{\partial v}{\partial x}\right) & \dfrac{\partial v}{\partial y} \end{bmatrix} \tag{18}$$

The two velocity components in Cartesian coordinates are denoted in Eqs.(17-18) with u and v. The u-velocity gradients can be calculated as follows [69]:

$$\left(\frac{\partial u}{\partial x}\right)_i = \sum_j \frac{m_j}{\rho_j}(u_j - u_i)\frac{(x_i - x_j)}{|\boldsymbol{r}_{ij}|}\frac{\mathrm{d}W}{\mathrm{d}\boldsymbol{r}_{ij}} \tag{19}$$

$$\left(\frac{\partial u}{\partial y}\right)_i = \sum_j \frac{m_j}{\rho_j}(u_j - u_i)\frac{(y_i - y_j)}{|\boldsymbol{r}_{ij}|}\frac{\mathrm{d}W}{\mathrm{d}\boldsymbol{r}_{ij}} \tag{20}$$

where $\boldsymbol{r}_{ij} = \boldsymbol{r}_i - \boldsymbol{r}_j$. Similar relations can be written for derivatives of the v-velocity component. To apply the above relations to SPH equations, we should obtain the full derivative between two particles using finite-differences.

After combining the above relations, the viscous (shear stress) term can be written as follows [70]:

$$\left(\frac{1}{\rho}\nabla\cdot\tau\right)_i = \left(\frac{\mu}{\rho}\nabla^2\mathbf{V}\right)_i = \sum_j \frac{4m_j(\mu_i - \mu_j)\boldsymbol{r}_{ij}\cdot\nabla_i W_{ij}}{(\rho_i + \rho_j)^2\left(|\boldsymbol{r}_{ij}|^2 + \eta^2\right)}(\mathbf{V}_i - \mathbf{V}_j) \tag{21}$$

To avoid division by zero, the value of $\eta = 0{,}1h$ is used. After substitution of Eq. (21) into the starting Eq. (3), the following expression is obtained [68]:

$$\frac{\mathrm{D}\mathbf{V}_i}{\mathrm{D}t} = -\sum_j m_j\left(\frac{P_i}{\rho_i^2} + \frac{P_j}{\rho_j^2}\right)\cdot\nabla_i W_{ij} + \mathbf{g} + \sum_j \frac{4m_j(\mu_i - \mu_j)\boldsymbol{r}_{ij}\cdot\nabla_i W_{ij}}{(\rho_i + \rho_j)^2\left(|\boldsymbol{r}_{ij}|^2 + \eta^2\right)}(\mathbf{V}_i - \mathbf{V}_j) \tag{22}$$

The description of the method continues with the presentation of the procedure for the approximation of viscous terms for the non-Newtonian fluid.

2.4. *A brief introduction to a rheological model*

Carreau proposed the following model for Pseudoplastic fluids in 1972 [48]:

$$\frac{\mu_{eff}(|\mathbf{D}|) - \mu_\infty}{\mu_0 - \mu_\infty} = [1 + (\lambda|\mathbf{D}|)^2]^{(n-1)/2} \tag{23}$$

The model is based on the molecular network theory. It has four parameters: μ_∞ - the viscosity at the infinite shear strain rate, μ_0 - the viscosity at the zero shear strain rate, λ and n. The value of parameter n, which is a time constant in the model, is generally greater than 1. For n = 1 Carreau-Yasuda model reduces to the model for Newtonian fluid.

The most important feature of this model is the use of viscosity at zero and infinite shear strain rates. Previous research [58] has shown that there is a significant difference between numerical simulation results and measurements when the fluid vicosity is modeled by the power-law, especially in regions with low and high shear strain rates. The rheological model of Carreau-Yasuda, which has these four parameters, overcomes this weakness of the power-law model in predicting the viscosity at the two limit states. Moreover, this model can predict the behavior of pseudoplastic fluids more accurately and in the range of shear rates.

2.5. *Solution algorithm*

A fully explicit three-step algorithm is proposed in this section. An algorithm that shows the sequence of computational steps for each term in the governing equations is presented in Fig. 1.

In *the first step*, the momentum equation is solved in the presence of the body forces while neglecting all other forces. As a result, an intermediate velocity is computed based on the solution from the previous time-step (subscript *t*):

$$u_* = u_t + g_x \Delta t \tag{24}$$

$$v_* = v_t + g_y \Delta t \tag{25}$$

Here $\mathbf{g} = (g_x, g_y)$ is the gravity acceleration. Our experience has shown that it is important to impose the body forces in the first step of the solution algorithm, especially in highly viscous fluids.

In *the second step*, the calculated intermediate velocities are employed to compute $|\mathbf{D}|$ followed by the computation of the divergence of the stress tensor. Note that the divergence of the stress tensor is a vector $\mathbf{S}$ given by:

$$\left(\frac{1}{\rho}\nabla \cdot \tau\right)_i = \mathbf{S} = S_x \vec{\imath} + S_y \vec{\jmath} \tag{26}$$

At the end of the second step, velocity components of each particle are updated according to:

$$u_{**} = u_* + S_x \Delta t = u_t + g_x \Delta t + S_x \Delta t \tag{27}$$

$$v_{**} = v_* + S_y \Delta t = v_t + g_y \Delta t + S_y \Delta t \tag{28}$$

At this stage, each particle is moved according to its intermediate velocity (u_{**}, v_{**}). Therefore, its intermediate position is given by:

$$x_* = x_t + u_{**} \Delta t \tag{29}$$

$$y_* = y_t + v_{**} \Delta t \tag{30}$$

where x_t and y_t are particle coordinates in the previous time-step. Thus far, no constraint has been imposed to satisfy the incompressibility of the fluid and it is expected that the density of some particles changes during this updating.

In *the third step* one can calculate the density variations for each particle using the continuity equation in the following form:

$$\frac{\mathrm{D}\rho_i}{\mathrm{D}t} = \sum_j m_j (\mathbf{V}_i - \mathbf{V}_j) \nabla_i W(\boldsymbol{r}_{ij}, h) \tag{31}$$

or

$$\frac{\mathrm{D}\rho_i}{\mathrm{D}t} = \sum_j m_j \mathbf{V}_{ij} \cdot \nabla_i W_{ij} \tag{32}$$

where ρ_i and $\mathbf{V}_i$ are the density and the velocity of particle i. When the two particles approach each other, the resulting effect is an increase in their density. This can be explained as follows. In either form of the continuity equation (31) or (32), the gradient of the Kernel function from Eq. (10) can be written as:

$$\nabla_i W_{ij} = \frac{\beta}{h^d} \begin{cases} -3(2-q)^2 + 12(1-q)^2 & 0 \le q \le 1 \\ -3(2-q)^2 & 1 \le q < 2 \\ 0 & q > 2 \end{cases} \tag{33}$$

When two particles approach each other, their non-dimensional distance is $0 \le q \le 1$, and thus the gradient of the Kernel function is negative. The contribution of particle *i* to the density of particle *j* in Eq. (32) is, according to Monaghan, 2005 [71]:

$$\rho_i \frac{m_j}{\rho_j} \mathbf{V}_{ij} \cdot \nabla_i W_{ij} \tag{34}$$

If particles *i* and *j* are approaching each other, the scalar product of vectors $\mathbf{V}_{ij} = \mathbf{V}_i - \mathbf{V}_j$ and $\nabla_i W_{ij}$ is $\mathbf{V}_{ij} \cdot \nabla_i W_{ij} > 0$. Thus, the contribution to the density change is positive as expected, i.e. $\mathrm{D}\rho_i/\mathrm{D}t$ will be positive. . Consequently, this will produce a repulsive force for approaching particles, i.e. $\boldsymbol{r}_{ij}$ will increase.

Similarly, if two particles are repulsed from each other, an attractive force will be

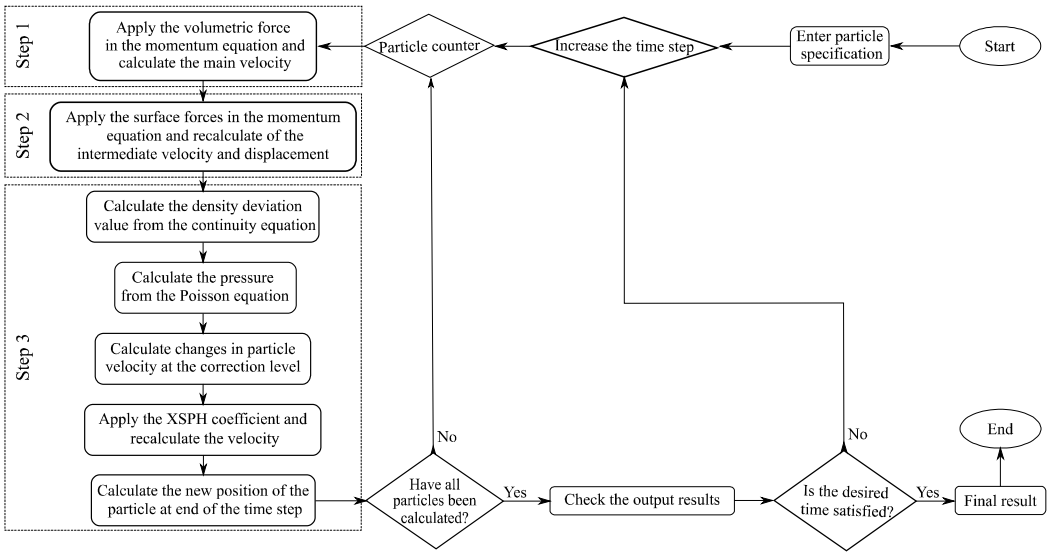

Fig. 1. General algorithm for solving fluid equations using an explicit three-step incompressible SPH method

produced to stop them from moving away. This interaction based on the relative velocity of particles and the resulting coupling between the pressure and density will enforce incompressibility condition in the solution procedure. The velocity field ($\hat{\mathbf{V}} = (\hat{u}, \hat{v})$) which is needed to restore the density of particles to their original value is now calculated. To do this, the velocity $\hat{\mathbf{V}}$ is fist defined from the momentum equation (3) in which all other terms, except the pressure gradient term, are neglected:

$$\hat{\mathbf{V}} = -\left(\frac{1}{\rho_*}\nabla P\right)\Delta t \tag{35}$$

where ρ_* is now the increased density of the particle after the predictor step, which does not satisfy continuity equation. Velocity $\hat{\mathbf{V}}$ is introduced into the discretised mass conservation equation for the compressible fluid:

$$\frac{1}{\rho_0}\frac{\rho_0 - \rho_*}{\Delta t} + \nabla \cdot \left(\hat{\mathbf{V}}\right) = 0 \tag{36}$$

where ρ_0 is the constant fluid density of the particle. After substitution of (35) into (36), the following pressure Poisson equation is obtained:

$$\nabla \cdot \left(\frac{1}{\rho_*}\nabla P\right) = \frac{\rho_0 - \rho_*}{\rho_0 \Delta t^2} \tag{37}$$

The Laplacian operator is presented with a dot product of the divergence and gradient operators as in [70]:

$$\nabla \cdot \left(\frac{1}{\rho}\nabla P\right)_i = \sum_j m_j \frac{8P_{ij}\, \boldsymbol{r}_{ij} \cdot \nabla_i W_{ij}}{\left(\rho_i + \rho_j\right)^2 \left(\left|\boldsymbol{r}_{ij}\right|^2 + \eta^2\right)} \tag{38}$$

where $P_{ij} = P_i - P_j$, while $\boldsymbol{r}_{ij}$ and η are the same as in Eqs. (20) and (21).
After substitution of Eq. (37) into Eq. (38), the pressure (P_i) for each particle is obtained by solving the combined equation:

$$P_i = \left(\frac{\rho_0 - \rho_*}{\rho_0 \Delta t^2} + \sum_j m_j \frac{8P_j\, \boldsymbol{r}_{ij} \cdot \nabla_i W_{ij}}{\left(\rho_i + \rho_j\right)^2 \left(\left|\boldsymbol{r}_{ij}\right|^2 + \eta^2\right)}\right) \cdot \left(\sum_j m_j \frac{8\, \boldsymbol{r}_{ij} \cdot \nabla_i W_{ij}}{\left(\rho_i + \rho_j\right)^2 \left(\left|\boldsymbol{r}_{ij}\right|^2 + \eta^2\right)}\right)^{-1} \tag{39}$$

The Eq. (39) is, actually, a system of equations that can be written in the matrix form. Its solution is therefore reached by solving the matrix equation. Once the pressure for each particle is known, one can calculate correction velocity vector $\hat{\mathbf{V}}_i$ from Eqs. (35) and (12):

$$\hat{\mathbf{V}}_i = -\Delta t \sum_j m_j \left(\frac{P_i}{\rho_{*i}^2} + \frac{P_j}{\rho_j^2} \right) \nabla_i W_{ij} \tag{40}$$

Finally, the velocity of each particle at the end of the time-step will be obtained as:

$$u_{t+\Delta t} = u_{**} + \hat{u} \tag{41}$$

$$v_{t+\Delta t} = v_{**} + \hat{v} \tag{42}$$

Additionally, the final position of particles is calculated using a central difference scheme in time:

$$x_{t+\Delta t} = x_t + \frac{\Delta t}{2}(u_{t+\Delta t} + u_t) \tag{43}$$

$$y_{t+\Delta t} = y_t + \frac{\Delta t}{2}(v_{t+\Delta t} + v_t) \tag{44}$$

This completes computations which are required for one time-step. The whole procedure is repeated in each time-step until a desired time is reached.

2.6. *The time step*

One can use the following formula to choose the appropriate time step Δt:

$$\Delta t = \alpha \min(\Delta t_1, \Delta t_2) \tag{45}$$

where $0 < \alpha < 1$ is a constant and

$$\Delta t_1 = \frac{h}{c + V_{\max}} \tag{46}$$

$$\Delta t_2 = \frac{h^2}{\mu_{eff}/\rho} \tag{47}$$

In the previous equation $V_{\max}$ is the maximum value of kinematic velocities of all phases and h is the distance between neighbouring particles. The first expression for the time-step (Δt_1) is the well known Courant–Friedrichs–Lewy condition. The other expression for Δt_2 is the stability condition for a parabolic equation when its derivatives are discretized explicitly and has arisen here from the viscous terms in the Navier–Stokes Eq. (12). This constraint of the time step was proposed by Shao and Lo, 2003 [70]. With the exception of deficient Reynolds numbers flows, the dominant condition is that from Eq. (46).

2.7. *Boundary conditions*

2.7.1. Solid Boundary conditions

Boundary particles are considered as the most elemental frontier particles that were invented in the initial applications of the SPH method. The particle layout is similar to the one which is shown in Fig. 2.

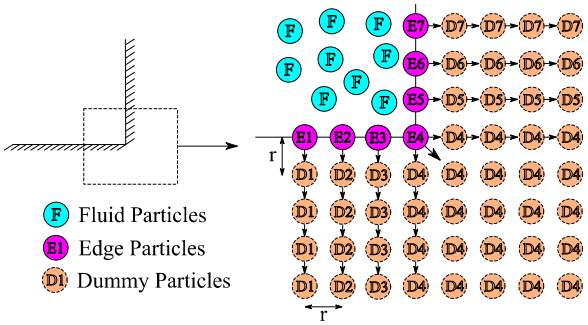

Fig. 2. The solid boundary condition applied in this study. Modeling of an external corner.

At first, a series of particles, whose density is similar to that of fluid particles, is arranged around the fluid flow region, as edge particles (E-particles). The velocity of E- particles is zero. Thus, they are not updated during simulation. Since they have physical properties such as density and this zero velocity, their

presence can speed-up computation and reduce simulation costs by saving the properties associated with these particles at the end of each step.

The number of virtual, dummy particle (D-particle) layers depends on the radius of the supporting zone *h*. The radius of this region is selected in such a way that the Kernel function on the solid boundary contains sufficient number of virtual particle layers. By using this approach, the error rate of the Kernel function on the boundary will have less effect on fluid particles.

In this type of solid-state modeling, the particle size of the virtual, D-particle is equal to the pressure of the particle on the corresponding edge. The pressure transfer from the fluid particle to the virtual particle at other locations such as corners or curved lines is slightly different.

2.7.2. Free surface boundary condition

When a fluid particle is placed on the free surface (*s*-particle in Fig. 3), its density decreases significantly compared to the density of fluid, internal particles (*i*-particles). The density reduction of a particle can be used as an indicator that a particle is located at the free-surface. In other words, all particles which fulfill the following condition [10]:

$$\rho^* < \beta_1 \rho_0 \tag{48}$$

are considered as particles at the free-surface, and a zero pressure is imposed on them. In the above relation ρ^* is the particle density in the predictor step, ρ_0 is the constant fluid density, and β_1 is the free surface parameter.

Eq. (48) cannot be directly used to calculate the pressure gradient for free-surface particles, given that there is no longer a particle on the other side of the free boundary, and a number of virtual particles should be considered. Thus, a virtual, mirror particle *m* is introduced in addition to *i*- and *s*-particles (Fig. 3). The virtual *m*-particle should be positioned along the line connecting *i* and *s*-particles at the distatance from particle *i* equal to the doubled distance between *i* and *s*-particles. Positions of these particles are depicted in Fig. 3.

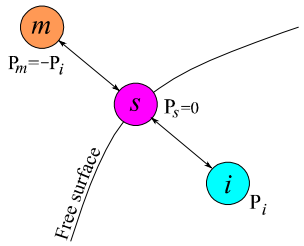

Fig. 3. The free-surface boundary condition and relation between internal, mirror and free-surfaces particles [10].

As it is shown in Fig. 3, the pressure from internal, *i*-particle is applied to the virtual particle *m* with the negative sign. In this manner, the zero pressure for the particle on the free-surface is obtained by interpolation between these two equal values with the opposite sign.

The pressure gradient between the free surface, *s*-particle, the virtual, *m*-particle and the internal, *i*-particle is calculated as follows:

$$\left(\frac{1}{\rho}\nabla P\right)_s = m_i\left(\frac{P_s}{\rho_s^2}+\frac{P_i}{\rho_i^2}\right)\nabla_s W_{si} + m_m\left(\frac{P_s}{\rho_s^2}+\frac{P_m}{\rho_m^2}\right)\nabla_s W_{sm} \tag{49}$$

We note here that all particles have the same mass, i.e. $m_s = m_i = m_m$. The gradient between the particles *s* and *i* is equal to the gradient between the particles *m* and *s*:

$$\begin{aligned} P_m &= -P_i \\ P_s &= 0 \\ \nabla_s W_{sm} &= -\nabla_s W_{si} \end{aligned} \tag{50}$$

After substitution of Eq. (50) into Eq. (49) one obtains:

$$\left(\frac{1}{\rho}\nabla P\right)_s = 2m_s\frac{P_i}{\rho_i^2}\nabla_s W_{si} \tag{51}$$

As a result, the actual gradient of pressure for the free-surface particle doubles, and it is possible to move the free-surface particle properly by applying these conditions. Since the Poisson equation for free-surface particles is not solved, this method does not apply to the incompressible condition for free-surface

particles. According to Eq. (51), there will be instabilities in the numerical solution for these particles. To solve this problem, the Laplace equation for the pressure is used between the free-surface, *s*-particle and the internal particle *i* [10]:

$$\nabla \cdot \left(\frac{1}{\rho}\nabla P\right)_s = 2\left(m_s \frac{8}{(\rho_s + \rho_i)^2} \frac{P_{si}\, \boldsymbol{r}_{si}.\nabla_s W_{si}}{|\boldsymbol{r}_{si}|^2 + \eta^2}\right) \tag{52}$$

By applying this equation, an uncontained condition for free-surface particles is applied. It should be noted that virtual particles do not enter into calculations of the shear stresses. Therefore, only particles below the free surface can produce shear forces, and the boundary condition of the zero sheer force at the free surface is satisfied in this way.

3. Validation of the proposed model

The proposed numerical model, based on the explicit three-step incompressible SPH method is tested first using the experimental data from three benchmark test cases:

- ✓ Dam-break simulation on the dry bed,
- ✓ Numerical modeling of impulse wave generated by rigid landslides and
- ✓ Pressure distribution of Carreau-Yasuda non-Newtonian fluid inside the tank under constant hydrostatic conditions

Consequently, the model is validated against numerical and laboratory data.

3.1. Dam-break simulation on the dry bed

The collapse of a fluid column on a horizontal surface, caused by a sudden removal of the retaining plate, i.e. the so called "dam-break", is a classical benchmark problem for the evaluation of free surface flow models. As one of the most straightforward free surface problems, this test case is chosen to assess the accuracy of the proposed explicit three-step incompressible SPH method.

Experimental data from [72] are used for the assessment. The layout for the numerical experiment is shown in Fig. 4. The problem is analysed in vertical, *x*0*z* plane.

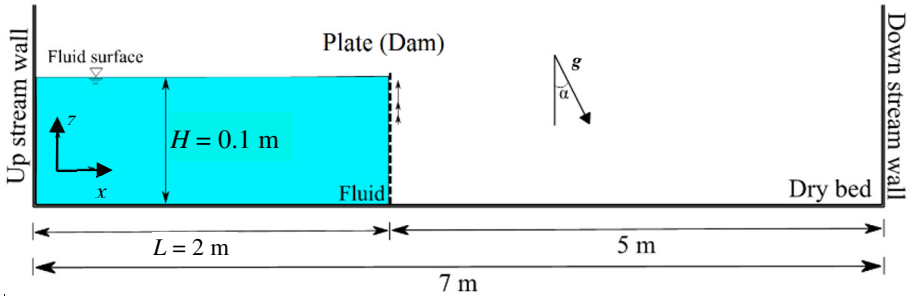

Fig. 4. Numerical model setup of the dam-break problem after Komatina and Jovanović, 1997 [72] (*L*: initial sample length, *H*: initial sample height).

A square sample (in blue in Fig. 4) with dimensions $L \times H$ is initially confined at the left side of a horizontal channel before the dam (the dashed line in Fig. 4) is removed to allow the collapse of the fluid column under the influence of gravity. The dam is modeled as a rigid and removable wall. The experiment with the channel bed slope of 0.1%, the initial column height of $H = 0.1$ m and the initial column width of $L = 2.0$ m is chosen for this study. The computational parameters used to solve the dam break problem are presented in Table 3. The dam is removed at time $t = 0$ s.

Table 3
Computational parameters for dam-break problem

$\rho_0(\mathrm{kg/m^3})$	$\mu(\mathrm{Pa \cdot s})$	$L_0(\mathrm{m})$	$h_0(\mathrm{m})$	$dt(\mathrm{s})$	*BP**	*FP**
1000	0.001	0.005	$1.5L_0$	0.00003	8000	8000

* BP: Boundary Particles (zone 0), FP: Fluid Particles (zone 1)

The smoothed length and the initial distance between particles are denoted by h_0 and L_0, respectively.

The advancement of the computed leading edge of the dam-break wave is compared to that observed in the experiment. The results are presented in Fig. 5 in non-dimensional form. The non-dimensional leading edge of the collapsing water column $(x - L)/H$ is plotted against the non-dimensional time $t/\sqrt{H/g}$.

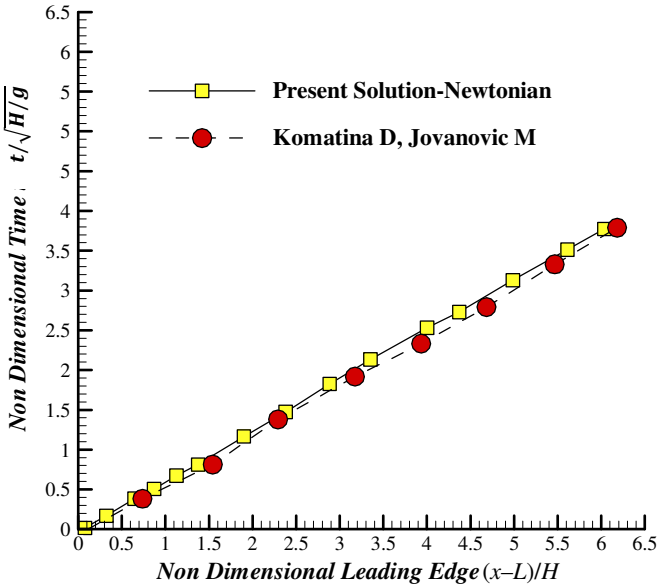

Fig. 5. Advancement of non-dimensional leading edge for the Newtonian Fluid – comparison of numerical simulation and experimental results

It is readily noticeable that the results of the proposed numerical model are in good agreement with measurements. The following statistics were used to assess model's performance for the Newtonian fluid: the correlation coefficient r in Eq. (53), the mean absolute error in Eq. (54), the root mean square error in Eq. (55), the efficiency coefficient of the Nash-Sutcliff model in Eq. (56) and the normalized root mean square error in Eq. (57). They are calculated for the flow depth at the dam-break site.

$$r = \frac{\sigma_{h_m h_p}}{\sigma_{h_m}\sigma_{h_p}} \tag{53}$$

$$MAE = \frac{1}{N}\sum_{i=1}^{N}\left(h_m - h_p\right) \tag{54}$$

$$RMSE = \sqrt{\sum_{i=1}^{N}\frac{\left(h_m - h_p\right)^2}{N}} \tag{55}$$

$$NSE = 1 - \frac{\sum_{i=1}^{N}\left(h_m - h_p\right)^2}{\sum_{i=1}^{N}\left(h_m - \bar{h}_m\right)^2} \tag{56}$$

$$NRMSE = \frac{RMSE}{\bar{h}_m} \tag{57}$$

where $\sigma_{h_m h_p}$ is the covariance, σ is the standard deviation, N is the number of data, h_m is the measured water depth, and h_p is the calculated water depth. Values of these statistics are given in Table 4.

Table 4
Values of statistics calculated for the assessment of the proposed model performance in the experiment of a dam-break over dry bed

r	*MAE*	*RMSE*	*NSE*	*NRMSE*

0.9998	0.0542	0.0003	0.974	0.168

As it can be seen, the agreement between the numerical model results and the experimental data is very good, which confirms the ability of the proposed model to successfully reproduce rapidly varying Newtonian flows.

3.2. Numerical modeling of impulse wave generated by rigid landslides

The second benchmark test case is that from Heinrich's laboratory study of submarine rigid landslides [49]. Experiments were performed in a 20 m long, 55 cm wide and 1.5 m deep channel at the Château National Hydraulic Laboratory in France. They involved the creation of water waves by the free-sliding motion of a rigid body on a 45° inclined plane. Fig. 6 shows the layout of the model at the beginning of the experiment.

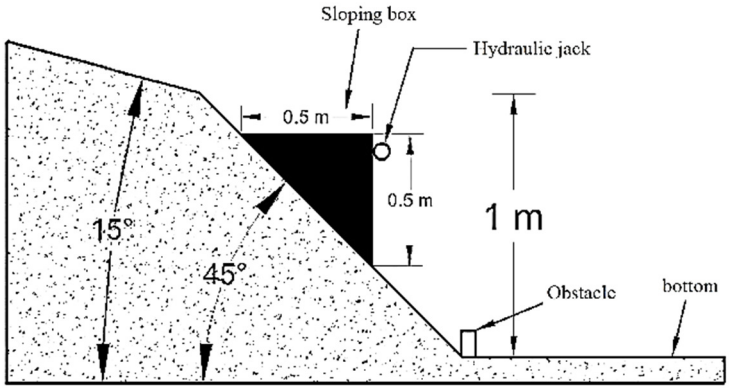

Fig. 6. Layout of the Submarine Landslide physical model [49]

The rigid body is a prism whose triangular base is half of the square with 0.5 m long edge. The prism height (a dimension perpendicular to the sketch) was adjusted to the width of the channel. The object was placed on four rollers. The hydraulic jack prevented the object to slide down the slope under the influence of gravity, while the plastic obstacle at the lee of the inclined plane was used to stop the object upon reaching the channel floor. After the release of the electrically controlled hydraulic jack, the object fell down the slope. The abrupt movement of the sliding rigid body produced waves on the free-surfce along the channel, whose profiles were recorded with a high speed camera. The soft surface of the object, the two sides of the slope, and the interior surface of the channel wall have been carefully treated to ensure their close agreement with the frictionless condition in numerical tests.

The water depth at rest was 1 m deep, which means that the rigid body was submerged at the beginning of the experiment. The weight of the object was 140 kg. The density of the fluid particles is 1000 kg/m^3 and the density of the material of which the sliding object was made is 2000 kg/m^3. Computational parameters that were used in numerical simulations of Heinrich's experiments are given in Table 5. The initial position and distribution of particles at $t = 0$ s are presented in Fig. 7.

Table 5
Computational parameters in the submarine rigid landslide problem

$\rho_0(\mathrm{kg/m^3})$	$\mu(\mathrm{Pa \cdot s})$	$L_0(\mathrm{m})$	$h_0(\mathrm{m})$	$dt(\mathrm{s})$	*BP**	*FP**	*OP**
1000	0.001	0.018	$1.5L_0$	0.00002	1240	8646	406

* BP: Boundary Particles (zone 0), FP: Fluid Particles (zone 1), Object Particles (zone 2)

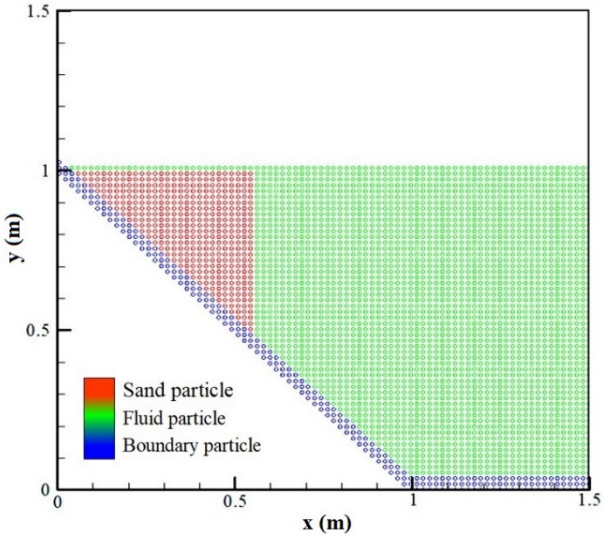

Fig. 7. Distribution of particles at $t = 0$ s

Fig. 8 illustrates measured against computed water levels at two time instants: $t = 0.5$ s and $t = 2$ s. The data collapse on the line of perfect fit with the following statistics: correlation coefficient $r = 0.95$ and $RMSE = 0.0071$. This proves high accuracy of the proposed three-step explicit SPH method in simulating water surface profiles in the case of submarine rigid landslides.

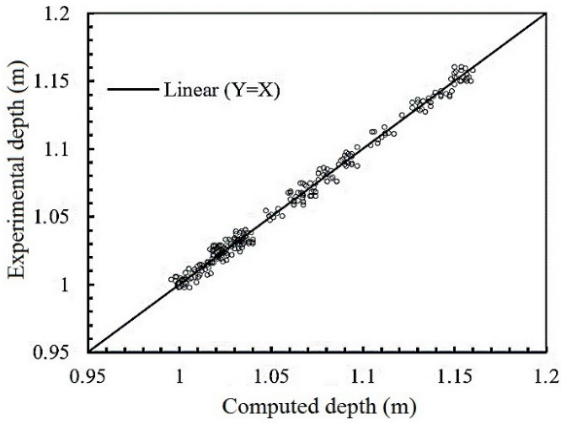

Fig. 8. Comparison of computed and measured water levels along the channel (results for the two time instants $t = 0.5$ s and $t = 2$s

3.3. Pressure distribution of Carreau-Yasuda non-Newtonian fluid inside the tank under constant hydrostatic conditions

The third issue to be addressed in this section is model's accuracy in the case of hydrostatic pressure distribution in the reservoir. Although the solution to such a problem is well known, many particle and Lagrangian methods are not able to solve this problem with acceptable accuracy. Modeling parameters for this type of problem are given in Table 6.

Table 6
Characteristics of Carreau-Yasuda non-Newtonian fluid and SPH parameters

dt (s)	h_0 (m)	L_0 (m)	μ_∞ (Pa · s)	μ_0 (Pa · s)	λ	n	ρ_{fluid} (kg/m^3)
0.00001	$1.5L_0$	0.018	5	135	0.036	0.9	800

A fluid having $\rho = 800$ kg/m^3 is at rest in a two-dimensional round tank with a diameter of 2 m and the depth of 0.5 m (Fig. 9). The three-step explicit incompressible SPH method is used to model the fluid in

the tank. Total duration of the simulation is 10 s. The initial distance between particles is $L_0 = 0.018$ m. At the start of simulation fluid particles inside the tank are only under the influence of the gravitational field, which is stationary, and the pressure is everywhere zero, i.e. $P(x, y, t = 0) = 0$. Initial distribution of particles is shown in Fig. 10. Red particles are fluid particles, whereas blue ones, that are distributed in 3 rows along the tank bottom and walls are solid boundary particles.

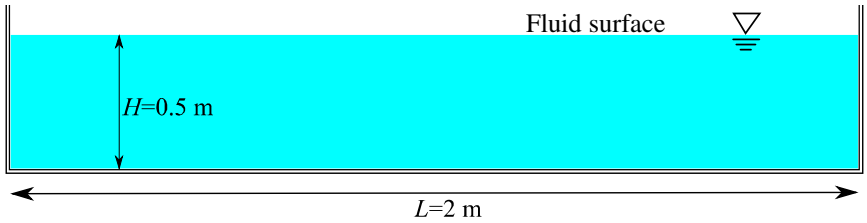

Fig. 9. Geometry in the hydrostatic tank problem

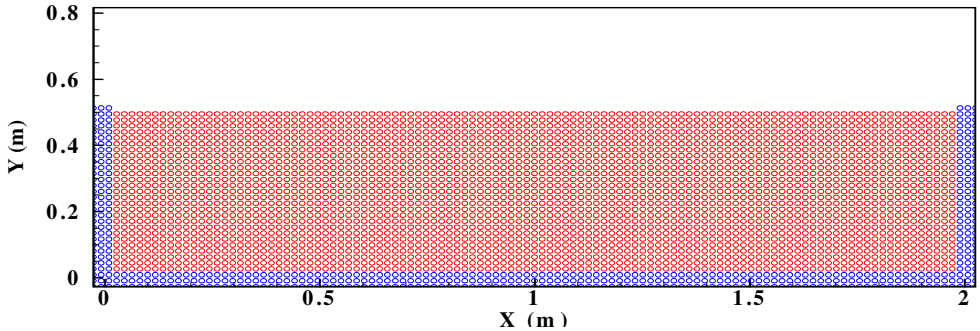

Fig. 10. Initial distribution of particles in the hydrostatic tank problem

Pressure distribution of the non-Newtonian Carreau-Yasuda fluid inside the tank at the end of simulation is shown in Fig. 11. It is readily noticeable that the relative pressure at the free surface is zero, and that it increases with depth. As it is expected, the pressure reaches its maximum value at the bottom of the tank. There is a slight difference in the pressure between the bottom and fluid particles at the tank corners. This can be explained by the behavior of the applied Kernel function at right angled corners.

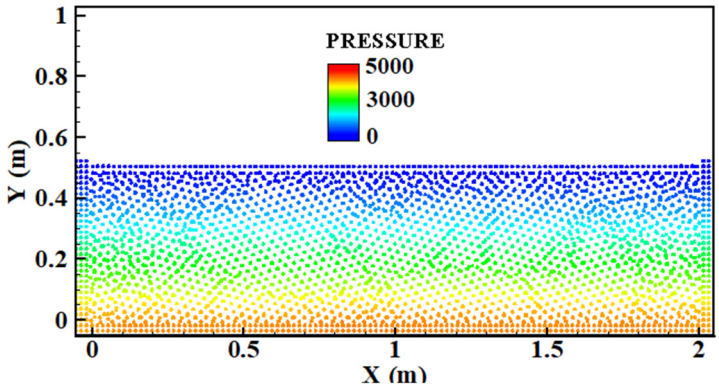

Fig. 11. Pressure distribution inside the tank filled with Carreau-Yasuda non-Newtonian fluid under constant hydrostatic conditions

4. Submarine non-rigid landslide

In this section performance of the proposed explicit three-step SPH method in modeling non-rigid landslide is assessed. Experiments of Rzadkiewicz et al. [56] that were previously used for the assessment

of other rheological models, i.e. Cross model by Ataie-Ashtiani et al. [10] and Bingham model by Capone et al. [58] are used here to assess Carreau-Yasuda model. The geometry of the computational domain is shown in Fig. 12. A triangular-base prism made of sand is allowed to slide down the 45° slope. Sides of the isoscale right triangle are 0.65 m long. Initial position of particles is shown in Fig. 13. The landslide movement has been simulated with the Carreau-Yasuda model, while the landslide interaction with water and the generated water waves have been simulated with the Newtonian model.

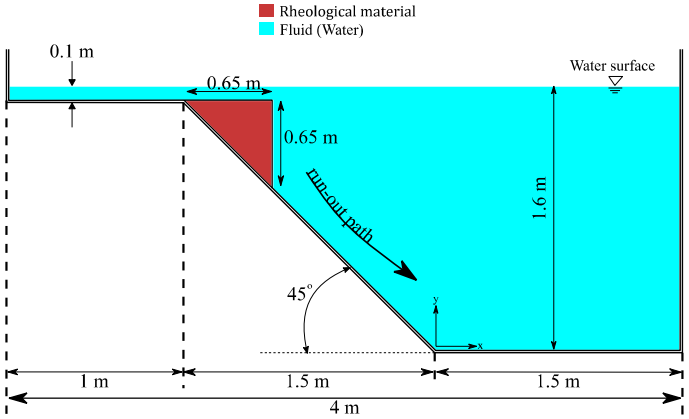

Fig. 12. Layout of the submarine non-rigid landslide model in experiments of Rzadkiewicz et al. [56]

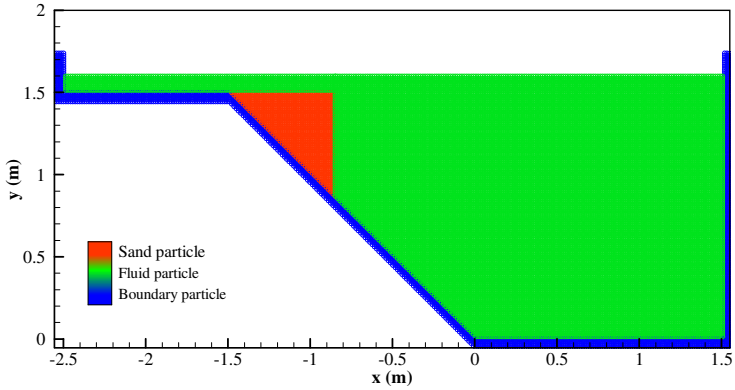

Fig. 13. Intial position of the three types of particles representing sand (red), fluid (green) and solid boundary (blue)

Due to a lack of the data, properties of the Carreau-Yasuda fluid were taken from [73]. They are listed in Table 7.

Table 7
Fluid properties for non-rigid landslide movement simulation

Description	Notation	Value
Water density	ρ_w (kg/m^3)	1000
Density of non-rigid body	ρ_o (kg/m^3)	800
Time interval	Δt (s)	0.00003
Water viscosity	μ (Pa s)	0.001
Viscosity of non-rigid body	μ_o (Pa s)	0.036
Infinite viscosity	μ_∞ (Pa s)	5
Zero viscosity	μ_0 (Pa s))	135
Power of the Carreau Yasuda equation	n	0.9

In addition to comparison with the experimental data, water surface profiles calculated in this study, are compared to those obtained by Ataie-Ashtiani et al. [10] and Capone et al. [58]. Fig. 14 shows these profiles at two time instants: $t = 0.4$ s and $t = 0.8$ s. Although there is a slight underestimation of water depths at the wave crest at $t = 0.4$ s and overestimation at $t = 0.8$ s, Carreau-Yasuda model with the three-step explicit incompressible SPH method performs better than the other two models along the falling limb at $t = 0.4$ s, and along the rising limb at $t = 0.8$ s (both for $x > 0.5$ m). These discrepancies can be attributed to different boundary conditions at the solid boundary in the laboratory and numerical experiments, i.e. to the different adhesion of the sand prism to the slanting plane, and to the uncertainty in the estimation of the viscosity of

the sliding non-rigid body. They are quantified using the L_2 relative error norm (ε_{L_2}) criterion [74]:

$$\varepsilon_{L_2} = \left(\frac{\sum_{i=1}^{N} (\Delta H)_i^2}{\sum_{i=1}^{N} (H)_i^2} \right)^{0.5} \tag{58}$$

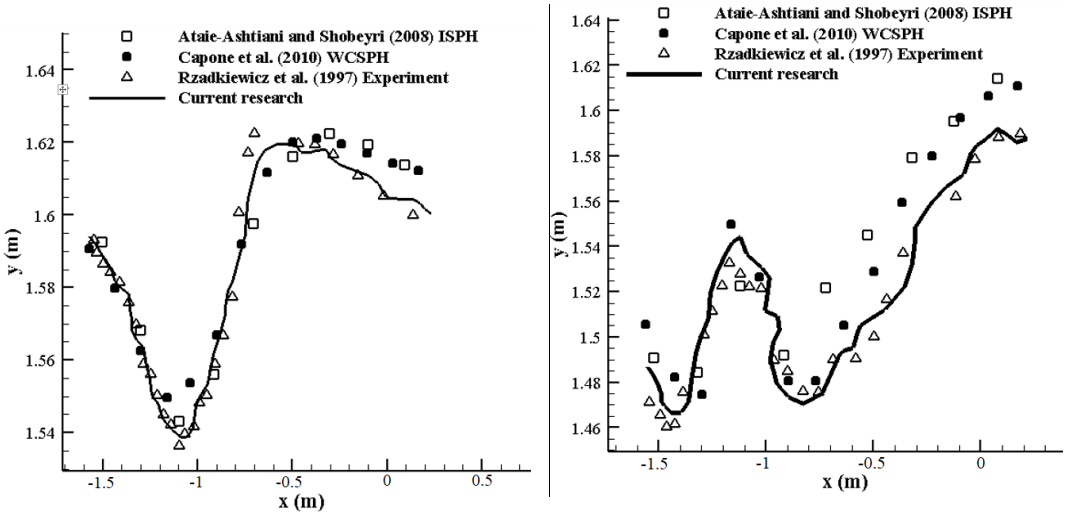

Fig. 14. Water surface profiles at t = 0.4 s (left) and at t = 0.8 s (right)

where ΔH is the difference between the free surface height in the laboratory experiment and that calculated by our model, while H is the measured free surface height in the laboratory model. The L_2 relative error norm is used for the assessment of both experimental and numerical responses.

In addition to (ε_{L_2}), values of other four statistics, given by equations (49)-(52), are available in Table 8 and Table 9 both for the Carreau-Yasuda rheological model used in this study, and Cross and Bingham models of Ataie-Ashtiani et al. [10] and Capone et al. [58], respectively. Results of comparison are given for the two time instants form Fig. 14.

Table 8
The values of Error Parameters at t = 0.4 s

Parameter	ε_{L_2}	*RMSE*	*NRMSE*	*MAE*	*NSE*
Ataie-Ashtiani and Shobeyri (2008) ISPH	0.0053	0.0065	0.0039	0.0018	0.9025
Capone et al. (2010) WCSPH	0.0071	0.0087	0.0055	0.0021	0.8724
Present study	0.00411	0.0051	0.0032	0.0011	0.9529

Table 9
The values of Error Parameters at times t = 0.8 s

Parameter	ε_{L_2}	*RMSE*	*NRMSE*	*MAE*	*NSE*
Ataie-Ashtiani and Shobeyri (2008) ISPH	0.0089	0.0112	0.0055	0.0022	0.8936
Capone et al. (2010) WCSPH	0.0078	0.0093	0.0069	0.0026	0.8824
Present study	0.00523	0.0063	0.0045	0.0018	0.9343

Results from the two tables clearly indicate that the Carreau-Yasuda model in combination with the proposed explicit three-step incompressible SPH method is superior to the other two models. Moreover, Fig. 15 shows that the proposed method with the Carreau-Yasuda rheological model is able to predict the advance of the collapsing non-rigid body accurately.

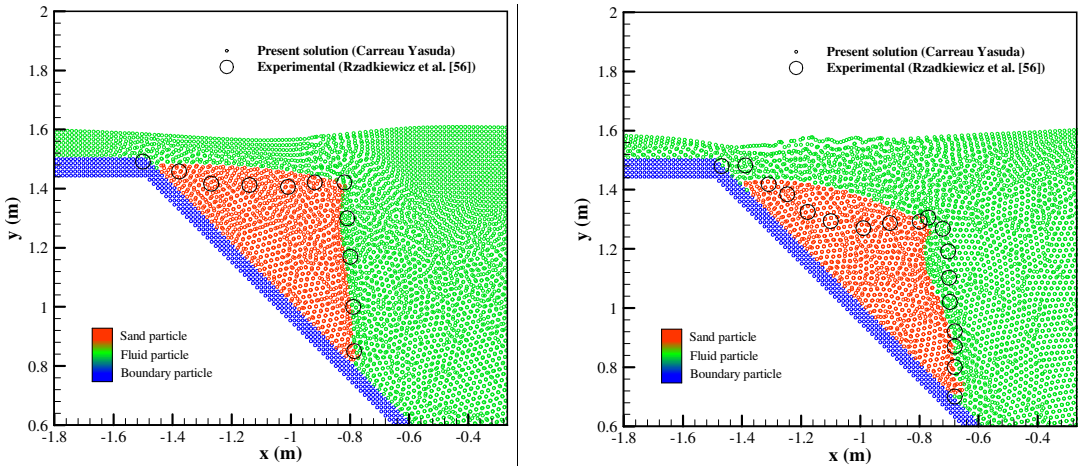

Fig. 15. Comparisons between sliding body profile calculated with SPH (red dots) and that measured by Rzadkiewicz et al. (1997) [56] (black circles), at $t = 0.4$ s (left) and $t = 0.8$ s (right)

There is also a slight difference in the shape of the crest of the non-rigid body between the model and the experiment. These differences were analysed by trial and error and have been evaluated by changing the values of the model parameters. One reason for this discrepancy is the lack of the information on the density of the non-rigid body in the experiment. Another reason is different adhesion of the sliding body to the inclined plane in the model and the experiment. There are no such data from the experiment, but it is believed that the adhesion in the laboratory model was greater than that in the numerical experiment. Additionally, no surface tension is included in the present calculations. Nevertheless, the model predicts the advancement of the non-rigid body correctly ($t = 0.4$ s and $t = 0.8$ s).

The chronological sequence of the landslide movement and accompanying development of waves on the free surface between $t = 0.1$ s and $t = 0.8$ s is shown in Fig. 16, at 0.1 s intervals. Changes on the free surface become apparent earlier ($t = 0.2$ s) than those in the shape of the sliding body ($t = 0.4$ s). Additionally, the shape of the crest does not change significantly after 0.6 s and a small bore is developed at the leading edge of the sliding body similar to that in gravity currents.

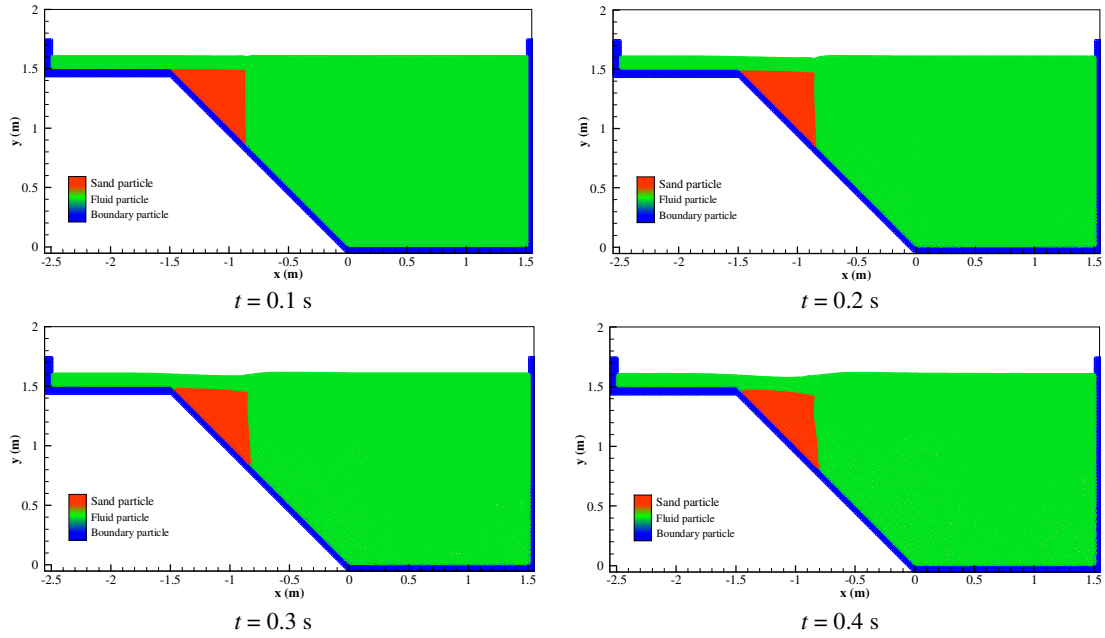

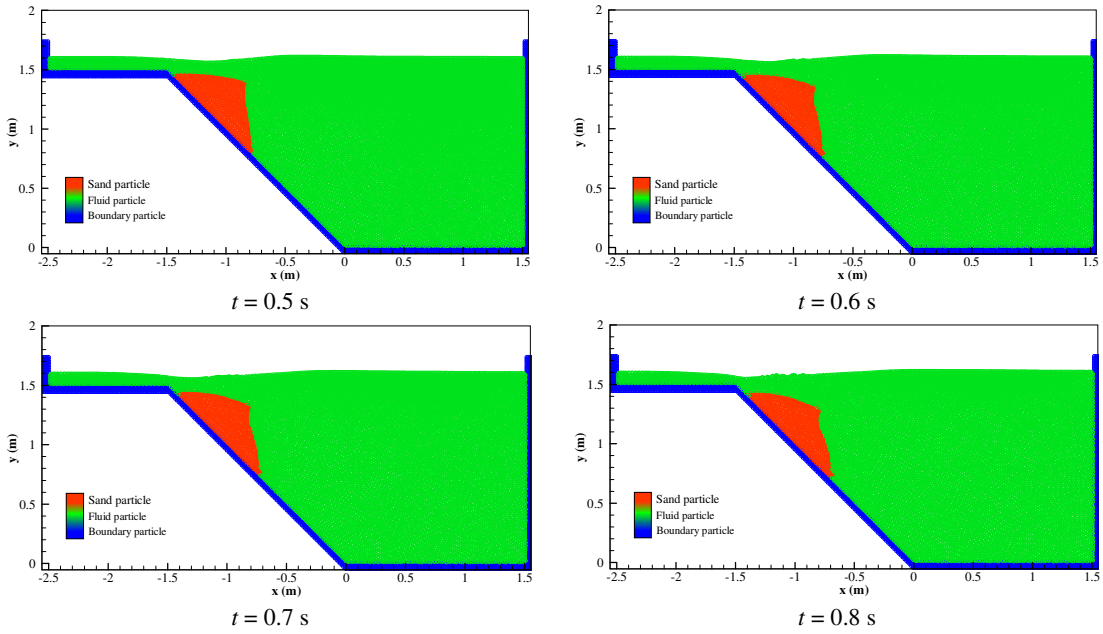

Fig. 16. Particle advancement in the non-Newtonian submarine landslide test

5. Conclusions

In this paper an improved explicit three-step incompressible SPH method is proposed for the simulation of non-rigid submarine landslides. The model is successfully tested for the Newtonian fluid on the dam-break and rigid body landslide benchmark test cases. Additonally, Carreau-Yasuda rheological model, that can predict the viscosity of psedoplastic fluids at low and high shear strain rate limits much better than the power-law model, is introduced in the analysis. In contrast to many Largangean and meshfree methods, the proposed combination of the improved SPH method and the Carreau-Yasuda rheological model can provide hydrostatic pressure distribution in the test case with the tank filled with Carreau-Yasuda fluid at rest.

This combination of the SPH method and the rheological model has not yet been used in SPH simulations of submarine landslides. Comparison of the calculated water surface disturbance caused by the submarine landslide with that obtained using the Cross model and ISPH model combination, or the one with Bingham and WCSPH models has shown that the proposed combination provides much better results than the other two. The L_2 relative error norm (ε_{L_2}), *RMSE* and *MAE* reduce by 20% to 70% when compared to the Cross model. In case of comparison with the Bingham model the reduction for L_2 relative error norm (ε_{L_2}) and *RMSE* is 40% to 70% while for the *MAE* the upper limit increases to 90%. The reduction of the *NRMSE* is rather stable (around 20%) when compared to the Cross model, while it varies in the range between 50% and 70% when the results are compared with those for the Bingham model. As for the *NSE*, the percentage reduction is stable in case of the Cross model (around 5%) and it is in the range between 5,5 and 8% in case of the Bingham model. Moreover, comparison with the experimental data indicates that the shape of the non-rigid body and its advancement down the inclined plane are captured well.

6. References

[1] Farhadi A. ISPH numerical simulation of tsunami generation by submarine landslides. Arabian Journal of Geosciences 2018;11(12): 330. https://doi.org/10.1007/s12517-018-3646-8

[2] Fritz HM, Mohammed F, Yoo J. Lituya Bay landslide impact generated mega-tsunami 50 th Anniversary. Tsunami Science Four Years after the 2004 Indian Ocean Tsunami: Springer; 2009. 153-75.

[3] Tan H, Xu Q, Chen S. Subaerial rigid landslide-tsunamis: Insights from a block DEM-SPH model. Engineering Analysis with Boundary Elements 2018;95: 297-314. https://doi.org/10.1016/j.enganabound.2018.07.013.

[4] Wang W, Chen G-q, Zhang H, Zhou S-h, Liu S-g, Wu Y-q, et al. Analysis of landslide-generated impulsive waves using a coupled DDA-SPH method. Engineering Analysis with Boundary Elements2016. 267-77. https://doi.org/10.1007/s11069-016-2171-x.

[5] Panizzo A, De Girolamo P, Di Risio M, Maistri A, Petaccia A. Great landslide events in Italian artificial reservoirs. Natural Hazards and Earth System Science 2005;5(5): 733-40.

[6] Froude MJ, Petley D. Global fatal landslide occurrence from 2004 to 2016. Natural Hazards and Earth System Sciences 2018;18: 2161-81. https://doi.org/10.5194/nhess-18-2161-2018.

[7] Fritz HM, Hager WH, Minor H-E. Landslide generated impulse waves. Experiments in Fluids 2003;35(6): 505-19. https://doi.org/10.1007/s00348-003-0660-7.

[8] Fritz H, Hager W, Minor H-E. Landslide generated impulse waves. 2. Hydrodynamic impact craters. Experiments in Fluids 2003;35(6): 520-32. https://doi.org/10.1007/978-3-0346-0064-4_9.
[9] Fritz H, Hager W, Minor H-E. Near field characteristics of landslide generated impulse waves. Journal of waterway, port, coastal, and ocean engineering 2004;130(6): 287-302. https://doi.org/10.1061/(ASCE)0733-950X(2004)130:6(287)
[10] Ataie-Ashtiani B, Shobeyri G. Numerical simulation of landslide impulsive waves by incompressible smoothed particle hydrodynamics. International Journal for numerical methods in fluids 2008;56(2): 209-32. https://doi.org/10.1002/fld.1526.
[11] Noda E. Water waves generated by landslides. Journal of the Waterways, Harbors and Coastal Engineering Division 1970;96(4): 835-55.
[12] Müller D, Schurter M. Impulse waves generated by an artificially induced rockfall in a Swiss lake. PROCEEDINGS OF THE CONGRESS-INTERNATIONAL ASSOCIATION FOR HYDRAULIC RESEARCH: LOCAL ORGANIZING COMMITTEE OF THE XXV CONGRESS; 1993. 209-09.
[13] Wang W, Zhang H, Zheng L, Zhang Y-b, Wu Y-q, Liu S-g. A new approach for modeling landslide movement over 3D topography using 3D discontinuous deformation analysis. Computers and Geotechnics 2017;81: 87-97. https://doi.org/10.1016/j.compgeo.2016.07.015.
[14] Wang W, Chen G, Zhang Y, Zheng L, Zhang H. Dynamic simulation of landslide dam behavior considering kinematic characteristics using a coupled DDA-SPH method. Engineering Analysis with Boundary Elements 2017;80: 172-83. https://doi.org/10.1016/j.enganabound.2017.02.016.
[15] Qiu L-c, Jin F, Lin P-z, Liu Y, Han Y. Numerical simulation of submarine landslide tsunamis using particle based methods. Journal of Hydrodynamics 2017;29(4): 542-51. https://doi.org/10.1016/S1001-6058(16)60767-9.
[16] Farhadi A, Emdad H, Rad EG. Incompressible SPH simulation of landslide impulse-generated water waves. Natural Hazards 2016;82(3): 1779-802. https://doi.org/10.1007/s11069-016-2270-8.[17] Ataie-Ashtiani B, Yavari-Ramshe S. Numerical simulation of wave generated by landslide incidents in dam reservoirs. Landslides 2011;8(4): 417-32. https://doi.org/10.1007/s10346-011-0258-8.
[18] Geist EL, Lynett PJ, Chaytor JD. Hydrodynamic modeling of tsunamis from the Currituck landslide. Marine Geology 2009;264(1-2): 41-52. https://doi.org/10.1016/j.margeo.2008.09.005.
[19] Watts P, Grilli S, Kirby J, Fryer G, Tappin D. Landslide tsunami case studies using a Boussinesq model and a fully nonlinear tsunami generation model. Natural Hazards And Earth System Science 2003;3(5): 391-402. https://doi.org/10.5194/nhess-3-391-2003.
[20] Bosa S, Petti M. Shallow water numerical model of the wave generated by the Vajont landslide. Environmental modelling & software 2011;26(4): 406-18. https://doi.org/10.1016/j.envsoft.2010.10.001.
[21] Quecedo M, Pastor M, Herreros M. Numerical modelling of impulse wave generated by fast landslides. International journal for numerical methods in engineering 2004;59(12): 1633-56. https://doi.org/10.1002/nme.934.
[22] Wroniszewski PA, Verschaeve JC, Pedersen GK. Benchmarking of Navier–Stokes codes for free surface simulations by means of a solitary wave. Coastal Engineering 2014;91: 1-17. https://doi.org/10.1016/j.coastaleng.2014.04.012.
[23] Fine I, Rabinovich A, Bornhold B, Thomson R, Kulikov E. The Grand Banks landslide-generated tsunami of November 18, 1929: preliminary analysis and numerical modeling. Marine Geology 2005;215(1-2): 45-57. https://doi.org/10.1016/j.margeo.2004.11.007.
[24] Heinrich P, Mangeney A, Guibourg S, Roche R, Boudon G, Cheminée JL. Simulation of water waves generated by a potential debris avalanche in Montserrat, Lesser Antilles. Geophysical Research Letters 1998;25(19): 3697-700. https://doi.org/10.1029/98GL01407.
[25] Viroulet S, Cébron D, Kimmoun O, Kharif C. Shallow water waves generated by subaerial solid landslides. Geophysical Journal International 2013;193(2): 747-62. https://doi.org/10.1093/gji/ggs133.
[26] Gingold RA, Monaghan JJ. Smoothed particle hydrodynamics: theory and application to non-spherical stars. Monthly notices of the royal astronomical society 1977;181(3): 375-89. https://doi.org/10.1093/mnras/181.3.375.
[27] Lucy LB. A numerical approach to the testing of the fission hypothesis. The astronomical journal 1977;82: 1013-24. https://doi.org/10.1016/j.coastaleng.2006.02.005.
[28] Shao S, Ji C, Graham DI, Reeve DE, James PW, Chadwick AJ. Simulation of wave overtopping by an incompressible SPH model. Coastal Engineering 2006;53(9): 723-35. http://dx.doi.org/10.1016/j.coastaleng.2006.02.005
[29] Pu JH, Shao S. Smoothed particle hydrodynamics simulation of wave overtopping characteristics for different coastal structures. The Scientific World Journal 2012;2012. https://doi.org/10.1100/2012/163613.
[30] Das R, Cleary P. Uniaxial compression test and stress wave propagation modelling using SPH. 2006.
[31] Das R, Cleary P. Modelling stress wave propagation and triaxial compression test using smoothed particle hydrodynamics. Proceedings of the 5th Australasian Congress on Applied Mechanics: Engineers Australia; 2007. 659. http://hdl.handle.net/102.100.100/129499?index=1.
[32] Antoci C, Gallati M, Sibilla S. Numerical simulation of fluid–structure interaction by SPH. Computers & Structures 2007;85(11): 879-90. https://doi.org/10.1016/j.compstruc.2007.01.002.
[33] Naili M, Matsushima T, Yamada Y. A 2D Smoothed Particle Hydrodynamics method for liquefaction induced lateral spreading analysis. Journal of applied mechanics 2005;8: 591-99. https://doi.org/10.2208/journalam.8.591.
[34] MAEDA K, SAKAI H, SAKAI M. Development of seepage failure analysis method of ground with smoothed particle hydrodynamics. Structural Engineering/Earthquake Engineering 2006;23(2): 307s-19s.
[35] Sakai H, Maeda K. Seepage failure and erosion mechanism of granular material with evolution of air bubbles using SPH. AIP Conference Proceedings: AIP; 2009. 1001-04. https://doi.org/10.1063/1.3179811.
[36] Takbiri Z, Rasekh A, Afshar MH. Analysis of seepage through dam foundation using smoothed particle hydrodynamics (SPH) meshless method. World Environmental and Water Resources Congress 2010: Challenges of Change2010. 1604-12. https://doi.org/10.1061/41114(371)169.
[37] Bui H, Nguyen C, Sako K, Fukagawa R. A SPH model for seepage flow through deformable porous media. The 5th International SPHERIC ConferenceGermany 2011: 164-71.
[38] Bui HH, Fukagawa R, Sako K, Ohno S. Lagrangian meshfree particles method (SPH) for large deformation and failure flows of geomaterial using elastic–plastic soil constitutive model. International Journal for Numerical and Analytical Methods in Geomechanics 2008;32(12): 1537-70. https://doi.org/10.1002/nag.688.

[39] Bui HH, Sako K, Fukagawa R, Wells J. SPH-based numerical simulations for large deformation of geomaterial considering soil-structure interaction. The 12th International Conference of International Association for Computer Methods and Advances in Geomechanics (IACMAG)2008. 570-78.
[40] Bui HH, Fukagawa R, Sako K, Wells J. Slope stability analysis and discontinuous slope failure simulation by elasto-plastic smoothed particle hydrodynamics (SPH). Geotechnique 2011;61(7): 565-74. https://doi.org/10.1680/geot.9.P.046.
[41] Bui HH, Fukagawa R. An improved SPH method for saturated soils and its application to investigate the mechanisms of embankment failure: Case of hydrostatic pore-water pressure. International Journal for numerical and analytical methods in geomechanics 2013;37(1): 31-50. https://doi.org/10.1002/nag.1084.
[42] Chen W, Qiu T. Numerical simulations for large deformation of granular materials using smoothed particle hydrodynamics method. International Journal of Geomechanics 2011;12(2): 127-35. https://doi.org/10.1061/(ASCE)GM.1943-5622.0000149.
[43] Opez Y, Roose D, Morfa CR. Dynamic refinement for SPH simulations of post-failure flow of non-cohesive soil. the 7th International SPHERIC Workshop2012.
[44] Hiraoka N, Oya A, Bui HH, Rajeev P, Fukagawa R. Seismic slope failure modelling using the mesh-free SPH method. International Journal of GEOMATE 2013;5(1): 660-65.
[45] Nguyen C, Bui HH, Fukagawa R. Two-dimensional numerical modelling of modular-block soil retaining walls collapse using meshfree method. Int J Geomate 2013;5(1): 647-52.
[46] Lemiale V, Mead S, Cleary P. Numerical Modelling of landslide events using a combination of continuum and discrete methods. Ninth international conference on computational fluid dynamics in the minerals and process industries, Melbourne, Australia2012.
[47] Wang J, Wu H, Gu C, Hua H. Simulating frictional contact in smoothed particle hydrodynamics. Science China Technological Sciences 2013;56(7): 1779-89. https://doi.org/10.1007/s11431-013-5262-x.
[48] Irgens F. Rheology and non-newtonian fluids: Springer; 2014.
[49] Heinrich P. Nonlinear water waves generated by submarine and aerial landslides. Journal of Waterway, Port, Coastal, and Ocean Engineering 1992;118(3): 249-66. https://doi.org/10.1061/(ASCE)0733-950X(1992)118:3(249).
[50] Monaghan J, Kos A, Issa N. Fluid motion generated by impact. Journal of waterway, port, coastal, and ocean engineering 2003;129(6): 250-59.
[51] Serrano-Pacheco A, Murillo J, García-Navarro P. A finite volume method for the simulation of the waves generated by landslides. Journal of hydrology 2009;373(3): 273-89. https://doi.org/10.1016/j.jhydrol.2009.05.003.
[52] Wenjie X. cel algorithm study of reservoir surge induced by landslide [J]. Journal of Engineering Geology 2012;3.
[53] Wang W, Chen G, Han Z, Zhou S, Zhang H, Jing P. 3D numerical simulation of debris-flow motion using SPH method incorporating non-Newtonian fluid behavior. Natural Hazards 2016;81(3): 1981-98. https://doi.org/10.1016/j.enganabound.2015.12.014.
[54] Khoolosi V, Kabdaşli S. Numerical Simulation of Impulsive Water Waves Generated by Subaerial and Submerged Landslides Incidents in Dam Reservoirs. Civil Engineering Journal 2016;2(10): 497-519. https://doi.org/10.28991/cej-2016-00000053.
[55] Heller V, Bruggemann M, Spinneken J, Rogers BD. Composite modelling of subaerial landslide–tsunamis in different water body geometries and novel insight into slide and wave kinematics. Coastal Engineering 2016;109: 20-41. https://doi.org/10.1016/j.coastaleng.2015.12.004.
[56] Rzadkiewicz SA, Mariotti C, Heinrich P. Numerical simulation of submarine landslides and their hydraulic effects. Journal of Waterway, Port, Coastal, and Ocean Engineering 1997;123(4): 149-57. https://doi.org/10.1061/(ASCE)0733-950X(1997)123:4(149).
[57] Mariotti C, Heinrich P. Modelling of submarine landslides of rock and soil. International journal for numerical and analytical methods in geomechanics 1999;23(4): 335-54. https://doi.org/10.1002/(SICI)1096-9853(19990410)23:4<335::AID-NAG974>3.0.CO;2-I.
[58] Capone T, Panizzo A, Monaghan JJ. SPH modelling of water waves generated by submarine landslides. Journal of Hydraulic Research 2010;48(S1): 80-84. https://doi.org/10.1080/00221686.2010.9641248.
[59] Shi C, An Y, Wu Q, Liu Q, Cao Z. Numerical simulation of landslide-generated waves using a soil–water coupling smoothed particle hydrodynamics model. Advances in Water Resources 2016;92: 130-41. https://doi.org/10.1016/j.advwatres.2016.04.002.
[60] Bose A, Carey G. Least-squares pr finite element methods for incompressible non-Newtonian flows. Computer methods in applied mechanics and engineering 1999;180(3-4): 431-58. https://doi.org/10.1016/S0045-7825(99)00177-2.
[61] Krishna MV, Reddy GS. MHD forced convective flow of non-Newtonian fluid through stumpy permeable porous medium. Materials Today: Proceedings 2018;5(1): 175-83. https://doi.org/10.1016/j.matpr.2017.11.069
[62] Monaghan JJ, Gingold RA. Shock simulation by the particle method SPH. Journal of computational physics 1983;52(2): 374-89. https://doi.org/10.1016/0021-9991(83)90036-0.
[63] Monaghan JJ. Smoothed particle hydrodynamics. Annual review of astronomy and astrophysics 1992;30(1): 543-74.
[64] Graham DI, Hughes JP. Accuracy of SPH viscous flow models. International journal for numerical methods in fluids 2008;56(8): 1261-69. https://doi.org/10.1002/fld.1619
[65] Liu G-R, Liu MB. Smoothed particle hydrodynamics: a meshfree particle method: World Scientific; 2003.
[66] Benz W. Smoothed particle hydrodynamics: A review. In numerical modeling of nonlinear stellar pulsation: Problems and prospects. Kluwer Academic Dordrecht 1990.
[67] Morris JP, Fox PJ, Zhu Y. Modeling low Reynolds number incompressible flows using SPH. Journal of computational physics 1997;136(1): 214-26. https://doi.org/10.1006/jcph.1997.5776.
[68] Cummins SJ, Rudman M. An SPH projection method. Journal of computational physics 1999;152(2): 584-607. https://doi.org/10.1006/jcph.1999.6246
[69] Hosseini S, Manzari M, Hannani S. A fully explicit three-step SPH algorithm for simulation of non-Newtonian fluid flow. International Journal of Numerical Methods for Heat & Fluid Flow 2007;17(7): 715-35. https://doi.org/10.1108/09615530710777976
[70] Shao S, Lo EY. Incompressible SPH method for simulating Newtonian and non-Newtonian flows with a free surface. Advances in water resources 2003;26(7): 787-800. https://doi.org/10.1016/S0309-1708(03)00030-7
[71] Monaghan JJ. Smoothed particle hydrodynamics. Reports on progress in physics 2005;68(8): 1703.
[72] Komatina D, Jovanovic M. Experimental study of steady and unsteady free surface flows with water-clay mixtures. Journal of Hydraulic Research 1997;35(5): 579-90. https://doi.org/10.1080/00221689709498395

[73] Chhabra RP, Richardson JF. Non-Newtonian flow and applied rheology: engineering applications: Butterworth-Heinemann; 2011.
[74] Shakibaeinia A, Jin Y-C. A mesh-free particle model for simulation of mobile-bed dam break. Advances in Water Resources 2011;34(6): 794-807. https://doi.org/10.1016/j.advwatres.2011.04.011